RESEARCH ARTICLE

Correspondence to:
L. J. Mazzaro,
laura.mazzaro@colorado.edu

Nested mesoscale-to-LES modeling of the atmospheric boundary layer in the presence of under-resolved convective structures

L. J. Mazzaro[1,2] [ID], D. Muñoz-Esparza[3] [ID], J. K. Lundquist[1,4] [ID], and R. R. Linn[2] [ID]

[1]Department of Atmospheric and Oceanic Sciences, University of Colorado, Boulder, Colorado, USA, [2]Los Alamos National Laboratory, Los Alamos, New Mexico, USA, [3]National Center for Atmospheric Research, Boulder, Colorado, USA, [4]National Renewable Energy Laboratory, Golden, Colorado, USA

Abstract Multiscale atmospheric simulations can be computationally prohibitive, as they require large domains and fine spatiotemporal resolutions. Grid-nesting can alleviate this by bridging mesoscales and microscales, but one turbulence scheme must run at resolutions within a range of scales known as the terra incognita (TI). TI grid-cell sizes can violate both mesoscale and microscale subgrid-scale parametrization assumptions, resulting in unrealistic flow structures. Herein we assess the impact of unrealistic lateral boundary conditions from parent mesoscale simulations at TI resolutions on nested large eddy simulations (LES), to determine whether parent domains bias the nested LES. We present a series of idealized nested mesoscale-to-LES runs of a dry convective boundary layer (CBL) with different parent resolutions in the TI. We compare the nested LES with a stand-alone LES with periodic boundary conditions. The nested LES domains develop $\sim$20% smaller convective structures, while potential temperature profiles are nearly identical for both the mesoscales and LES simulations. The horizontal wind speed and surface wind shear in the nested simulations closely resemble the reference LES. Heat fluxes are overestimated by up to $\sim$0.01 K m s^{-1} in the top half of the PBL for all nested simulations. Overestimates of turbulent kinetic energy (TKE) and Reynolds stress in the nested domains are proportional to the parent domain's grid-cell size, and are almost eliminated for the simulation with the finest parent grid-cell size. Based on these results, we recommend that LES of the CBL be forced by mesoscale simulations with the finest practical resolution.

1. Introduction

Wind energy production, flow over complex terrain, pollutant transport, and many other lower-atmosphere phenomena depend on large-scale weather patterns as well as small-scale flow structures. Accurately modeling all these scales requires a finely resolved, very large domain, which is computationally prohibitive. To circumvent this problem, the output from coarsely resolved, parent domains can be used as boundary conditions to smaller, fine resolution domains through grid-nesting. This technique can be used for mesoscale-to-microscale refinement [e.g., *Liu et al.*, 2011; *Talbot et al.*, 2012; *Mirocha et al.*, 2014; *Zhou and Chow*, 2013; *Muñoz-Esparza et al.*, 2014b; *Taylor et al.*, 2016; *Rai et al.*, 2016]. Often, a microscale, large eddy simulation (LES) domain is embedded within mesoscale simulations that are conducted at resolutions orders of magnitude higher than is recommended due to grid-refinement limitations. In the presence of convection, these high resolutions can violate the assumptions of the 1-D PBL schemes used by mesoscale models to model vertical turbulent diffusion. This results in unrealistic flow characteristics [*Honnert et al.*, 2011; *Beare*, 2013; *Zhou et al.*, 2014; *Ching et al.*, 2014; *Shin and Dudhia*, 2016]. In this study, we quantify the effect of these unrealistic convective flows on a nested LES, to determine whether they can influence the development of the nested LES flow.

Atmospheric models have developed in two separate branches based on two different scales of motion. For mesoscale and synoptic-scale processes, mesoscale and general circulation models are used for numerical weather prediction and to improve our understanding and future projections of our planet's climate. These models are designed to use large grid-cell sizes ($\Delta x \sim$10–100 km) and they are usually performed over very large domains. For microscale motions, models such as LES use much finer resolutions ($\Delta x \sim$1–10 m) to resolve turbulence within the inertial range. The range of scales between these two extremes ($\Delta x \sim$10 m–10 km) was

defined by *Wyngaard* [2004] as the terra incognita (TI), often referred to as the "gray zone" [*Beare*, 2013; *Zhou et al.*, 2014; *Efstathiou and Beare*, 2015; *Honnert et al.*, 2016; *Shin and Dudhia*, 2016], where mesoscale and also microscale model assumptions break.

As numerical resources continue to advance, it is becoming more common to perform large-domain, mesoscale simulations at TI resolutions [*Cheng et al.*, 2010; *Miyamoto et al.*, 2013; *Wing and Emanuel*, 2014]. In doing so, under many atmospheric conditions, mesoscale model assumptions are violated resulting in model inaccuracies [*Zhou et al.*, 2014; *Ching et al.*, 2014; *Shin and Dudhia*, 2016; *Honnert et al.*, 2016]. This problem is especially manifested in cases where atmospheric convection is present.

In the presence of strong surface heat-fluxes, convectively induced updrafts and downdrafts can organize and combine as convective rolls or cells. This phenomenon is known as convective aggregation. Convective aggregation can present particular challenges when modeling at resolutions within the TI. Aggregated convective structures in the atmosphere are on the order of 1–5 km. Due to their scale, these structures are too fine to be fully resolved at traditional mesoscale grid-cell sizes. Mesoscale model parametrizations are designed with this in mind: by requiring horizontal statistical homogeneity within single grid-cells, these models assume that all of the convective structures and turbulent motions occur at subgrid scales (SGS). This assumption that no convective structures and turbulent motions are resolved is violated when the models are run at TI resolutions, which are on the same order as the structures and are thus able to partially resolve these motions. The under-resolved convective motions result in unrealistic grid-dependent structures in the flow [*Zhou et al.*, 2014; *Ching et al.*, 2014]. Additionally, since mesoscale parametrizations do not take into account the resolved turbulent energy, they can misrepresent the large-scale influence of the partially parametrized processes [*Sullivan and Patton*, 2011; *Honnert et al.*, 2011; *Zhou et al.*, 2014; *Ching et al.*, 2014; *Shin and Dudhia*, 2016; *Honnert et al.*, 2016].

Previous studies have analyzed the effect of the mesoscale assumption violations on modeled convective flows at TI resolutions. In a study with strong convection (convective cells) *Zhou et al.* [2014] showed that first-order flow statistics, such as mean potential temperature profiles, did not change with resolution in the TI, while the modeled vertical heat flux in the TI runs was higher than the vertical heat flux of the filtered LES domain, making resolved convection more energetic in the TI than predicted by the control simulations. *Ching et al.* [2014] found that additional turbulent mixing in the TI made virtual temperature profiles more neutral, which in turn can delay or suppress the growth of modeled convective structures. In a more recent study for flows containing convective cells, *Shin and Dudhia* [2016] confirmed that first-order statistics do not vary significantly with resolution, while turbulent statistic variations depend on both mesoscale resolution and the choice of PBL scheme. They found that for the Mellor-Yamada-Nakanishi-Niino (MYNN) level-2.5 PBL scheme [*Nakanishi and Niino*, 2009], both the resolved vertical heat transport and the magnitude of the vertical momentum transport are greater than the reference filtered-LES transports.

Coupling between mesoscale and microscale models through grid-nesting allows us to perform a fine-resolution, small-domain simulation while still considering the large-scale characteristics of the flow. The small domain, known as the nested domain, is located over a region of interest and bounded by conditions from a coarser, larger-domain, known as the parent domain. Grid-nesting between mesoscale and microscale resolutions results in $\phi = \Delta x_{parent}/\Delta x_{nest} \sim 100$. However, such high grid-refinement ratios, ϕ, are not recommended, since such sudden increase in terrain complexity resolution can produce large gradients that unrealistically affect the nested domain [*Warner et al.*, 1997]. To use a lower ϕ, mesoscale-to-microscale nesting is usually performed with one of the models at TI resolution. Recently, *Muñoz-Esparza et al.* [2017] have shown that the presence of under-resolved convection originated at fine resolution mesoscale model simulations imposes artificial structures that delay the onset of turbulence and degrades the performance of nested mesoscale-LES simulations of real conditions. Motivated by these findings, in this study we focus on the effect of unrealistic TI mesoscale flows on a nested LES domain. This setup is most useful for applications that require highly resolved microscale information, for example, wind energy forecasting [*Calaf et al.*, 2010; *Porte-Agel et al.*, 2011; *Aitken et al.*, 2014; *Vanderwende et al.*, 2016], flow over complex terrain [*Michioka and Chow*, 2008; *Chow and Street*, 2009; *Fernando*, 2010; *Lundquist et al.*, 2012; *Zhou and Chow*, 2013; *Sauer et al.*, 2016; *Rai et al.*, 2016] and pollutant transport [*Fernando et al.*, 2001; *Lundquist et al.*, 2012; *Taylor et al.*, 2016].

By comparing a reference stand-alone LES with three nested LES domains bounded by mesoscale parents at different TI resolutions, we can quantify the effect of the parent characteristics on the nested flows. In section 2, the numerical setup and simulations are described, and an analysis is provided justifying how the data are cropped for computing statistics. Section 3 has a detailed comparison of the simulated flows. The parent flow characteristics are described, and the nested flow is compared to the reference, stand-alone LES. Comparisons are made on the basis of spatial turbulence development, first-order flow characteristics, turbulence characteristics, turbulent partitioning between the vertical and horizontal directions, and the length scales of the resolved convective structures. Section 4 contains a summary of the observations made in the analysis, as well as recommendations for the optimal observed setup and suggestions for future studies.

2. Numerical Setup

We perform three idealized, one-way nested, mesoscale-to-LES runs for a dry CBL with different parent TI resolutions, summarized in Table 1. The nested domains are centered in the horizontal dimensions x and y within their respective parent domains. The nested flows are compared with a reference, stand-alone LES to assess the effect of the spurious structures in the parent domains. The differences between the nested and stand-alone flows represent the bias caused by the unrealistic structures present in the mesoscale flows.

The simulations are performed using the Weather Research and Forecasting (WRF) model version 3.6 [*Skamarock et al.*, 2008]. The nonlinear backscatter and anisotropy (NBA) scheme is used to model SGS mixing for the LES [*Kosović*, 1997; *Mirocha et al.*, 2010]. For SGS mixing in the mesoscale simulations, the MYNN scheme [*Nakanishi and Niino*, 2009] is used. The surface layer was modeled using the Monin-Obukhov similarity theory [*Monin and Obukhov*, 1954]. Coriolis effects are included through a Coriolis parameter of $f = 10^{-4}$ s^{-1}, corresponding to a latitude of 43.3°N. A constant geostrophic wind forcing is applied in the x direction, $(U_g, V_g) = (8.1, 0)$ m s^{-1}. Convection is produced by a constant sensible heat flux, $\langle w'\theta'\rangle_s = 0.08$ K m s^{-1}, applied at the surface. An initial potential temperature profile of 288 K through a PBL height of $z_i = 2000$ m is topped by a 150 m inversion of strength 0.08 K m^{-1} and a weaker inversion of strength 0.003 K m^{-1} through the rest of the domain height, up to $z_{top} = 3500$ m. A Rayleigh damping layer with a damping coefficient of 0.2 s^{-1} is applied through the top 500 m of the domain to ensure that no turbulent motions reached the top boundary of the simulations [*Klemp et al.*, 2008]. The same vertical resolution is used for all of the simulations, thus not considering the effects of vertical grid-refinement [*Daniels et al.*, 2016]. The mesoscale simulations are spun up for 4 h, then the nested LES are initialized and spun up for 3 h. After this, 3 h of data are output at 1 min intervals. These spin-up times were determined from the temporal evolution of horizontally averaged TKE at different heights. Figure 1 shows the time evolution of TKE for all of our simulations at a height $z = 1000$ m.

A stand-alone LES with periodic boundary conditions serves as a reference flow, uncontaminated by the influence of the mesoscale modeled structures. This simulation with a timestep, $\Delta t = 0.4$ s, and a horizontal grid-cell size of $\Delta x = \Delta y = 47.57$ m and a vertical grid-cell size of $\Delta z = 20$ m. The size of the domain is

Table 1. Simulation Setup Including Parent Domains for the Nested Simulations, Grid-Size ($\Delta x, y, z$), Horizontal Domain Size (L_x, L_y), SGS Scheme and Whether or Not the Cell-Perturbation Method Was Implemented in the Nested Domains

|	Label	Parent	$\Delta x, \Delta y$ (m)	Δz (m)	SGS Scheme	L_x [km]	L_y [km]	Cell Perts.
Stand-alone	p_{ref}		47.57	20	NBA	50	20	
Parent	p_{333}		333	20	MYNN	63	33	
Nest	n_{333}	p_{333}	47.57	20	NBA	50	20	Yes
Nest	n_{333np}	p_{333}	47.57	20	NBA	50	20	No
Parent	p_{666}		666	20	MYNN	127	67	
Nest	n_{666}	p_{666}	47.57	20	NBA	50	20	Yes
Nest	n_{666np}	p_{666}	47.57	20	NBA	50	20	No
Parent	p_{999}		999	20	MYNN	190	100	
Nest	n_{999}	p_{999}	47.57	20	NBA	50	20	Yes
Nest	n_{999np}	p_{999}	47.57	20	NBA	50	20	No
Stand-alone	p_{2000}		2000	20	MYNN	382	202	
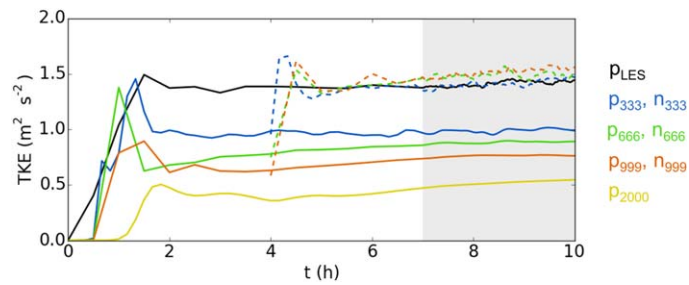
Figure 1. Horizontally averaged resolved TKE $= 2^{-1}(u'^2 + v'^2 + w'^2)$, at $z = 1000$ m for all simulations. The shaded gray area represents the time interval used for the analysis of the simulations [7–10 h]. Solid lines (—) represent periodic domains, with x-averaged conditions. Dashed lines (- - -) represent nested domains, for which statistics were found at $x = 40$ km. Descriptions for all the runs in the legend can be found in Table 1.

$(L_x, L_y) = (50, 20)$ km. The simulation is run for a 7 h spin-up period, after which 3 h of data were output at 1 min intervals. Horizontal contours of vertical velocity, w, and potential temperature, θ, at two different heights show the structure of the modeled convective cells (Figure 2).

Four mesoscale simulations are performed with a timestep, $\Delta t = 0.8$ s, and with different resolutions within the TI, $\Delta x_{meso} = 333$, 666, 999, and 2000 m, as summarized in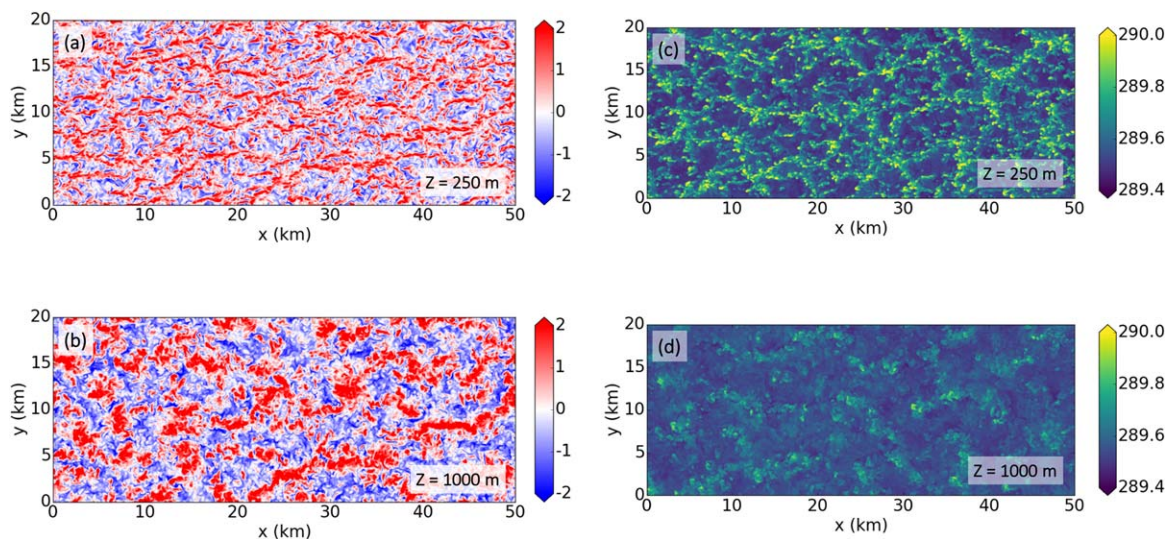 Table 1. The resolved flows from the first three of these simulations provide lateral boundary conditions to the grid-nested LES domains. The fourth mesoscale simulation was performed to show that the effects of the TI on mesoscale flows were present at even coarser resolutions. However, this simulation was not used as a parent domain since such a high ϕ would require a much larger nested LES domain in order to accurately sample the mesoscale flow heterogeneity through the LES boundary conditions. Such setup would be very computationally expensive, and was therefore considered to not be a practical application of this coupling technique.

Nested LES domains with the same resolution and timestep as the stand-alone LES domain ($\Delta x = 47.57$ m, $\Delta t = 0.4$ s) are centered within the three finest mesoscale simulations, (p_{333}, p_{666}, and p_{999}). One-way feedback is implemented so that the nested LES domains have no influence on the parent mesoscale domains. The domain of these LES is the same as that for the stand-alone LES, $(L_x, L_y) = (50, 20)$ km. The extent of this domain is greater than $5z_i$ in both the x and y direction, making it large enough to avoid the potential for mean temperature and vertical velocity bias between the parent and the nested domains [*Moeng et al.*, 2007]. Vertical grid-refinement is not considered, so both the parent and nested domains have the same vertical grid-cell size, $\Delta z = 20$ m. The three nested simulations correspond to $\phi = \Delta_{meso} / \Delta_{LES} = 7$, 14, 21. These values are higher than $\phi = 3$, which is traditionally used for mesoscale-to-mesoscale and LES-to-LES grid-nesting. A recommended ϕ has not yet been defined for mesoscale-to-LES grid-nesting applications, for which a higher ϕ could potentially help to avoid the use of TI resolutions [*Zhou and Chow*, 2013; *Taylor et al.*, 2016; *Rai et al.*, 2016; *Muñoz-Esparza et al.*, 2017].

Figure 2. Horizontal contours of (a, b) vertical velocity, w (m s^{-1}), and (c, d) potential temperature, θ (K), for two different heights (250 and 1000 m) for the stand-alone LES case after 10 h of simulation.

The cell perturbation method [*Muñoz-Esparza et al.*, 2014b, 2015] is applied near the inflow boundaries of the nested domain to generate realistic turbulence at the scales resolvable by the LES grid resolution. The perturbations are applied over two-dimensional, horizontal cells of size $(L_{px}, L_{py}) = (8\Delta x, 8\Delta y)$, over the first 24 cells of both inflow boundaries and at each vertical grid-cell for the bottom two-thirds of the PBL. The maximum potential temperature perturbation amplitude, $\tilde{\theta}_{pm} = 0.33$ K, corresponds to a perturbation Eckert number as proposed by *Muñoz-Esparza et al.* [2015], $Ec = U_g^2 (c_p \tilde{\theta}_{pm})^{-1} \approx 0.2$, where $c_p \approx 1.005$ kJ (kg K)$^{-1}$ is the specific heat capacity at constant pressure. The perturbation time step is $t_p = 115$ s, corresponding to a dimensionless time scale, $\Gamma = t_p U_1 d_c^{-1} \sim 1.3$, where $U_1 = [6.5, 6.6, 6.4]$ m s^{-1} for $[n_{333}, n_{666}, n_{999}]$ is the wind speed at the first vertical grid-point imposed on the LES boundary, and $d_c = 70.7$ m is the diagonal grid-cell length. The chosen perturbation Eckert number and dimensionless time scale are optimized values recommended by *Muñoz-Esparza et al.* [2015] for the fastest transition to fully developed turbulence. To highlight the effect of the cell perturbation method on the nested LES domains, we have performed a series of nested LES simulations without cell perturbations, for parent resolutions $\Delta x = [333, 666, 999]$m ($n_{333np}$, n_{666np}, n_{999np}). By comparing these unperturbed, modeled flows to the perturbed flows (n_{333}, n_{666}, n_{999}) we showcase the advantages of using cell perturbations for turbulence generation in the context of the present study.

Due to Coriolis effects, the direction of the mean simulated flow after spin-up is approximately 15° from the x direction. Because of this, there is a region near the $y = 0$ boundary of the nested domain in which the boundary conditions are evident (Figure 3). The extent of this region was determined from the evolution of resolved TKE in the nested domains (Figure 4). The resolved TKE of all three of the nested domains develops rapidly in the first 1500 m of the y direction and decreases to a stable value of ~ 1.5 m^2 s^{-2} by $y \sim 5000$ m. The analysis presented in the following sections does not include data from the first 5000 m of the y boundary, to avoid including any potential bias from these conditions.
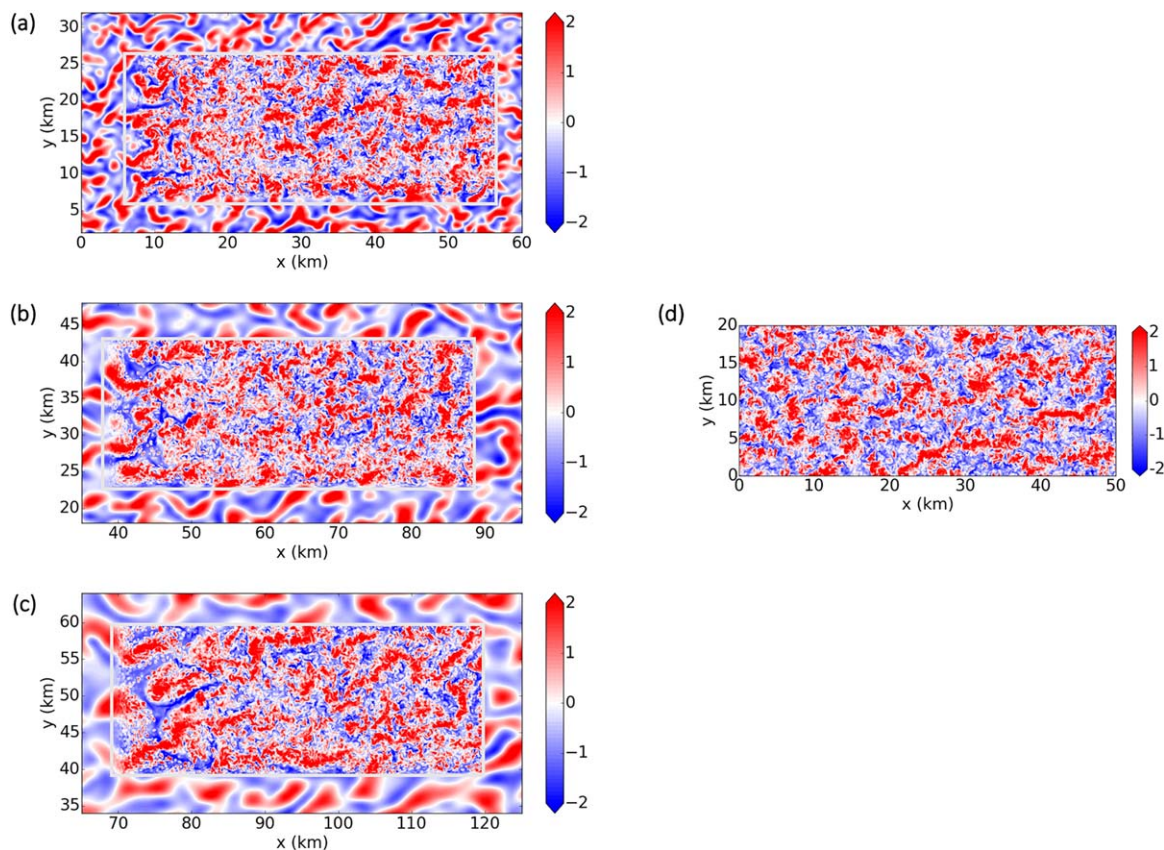

Figure 3. Horizontal contours of vertical velocity, w (m s^{-1}), at a height of $z = 1000$ m and after 10 h of simulation, for the nested simulations. The parent domain resolutions are $\Delta x =$ (a) 333 m (p$_{333}$), (b) 666 m (p$_{666}$), and (c) 999 m (p$_{999}$). Figure 3d shows the horizontal contour of w for the stand-alone LES (p$_{LES}$) at $z = 1000$ m. The white rectangles have been added to highlight the nested domain.
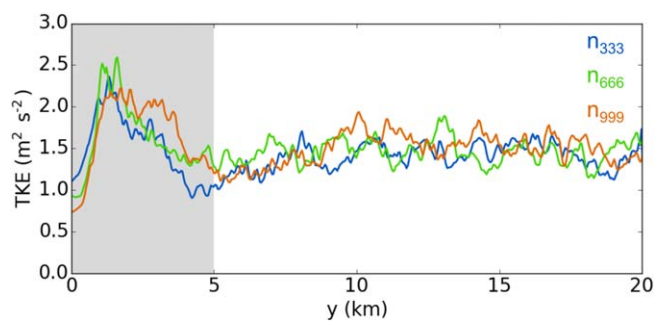
Figure 4. Temporally averaged resolved TKE as a function of y at $z = 1000$ m and $x = 40$ km for nested simulations (n_{333}, n_{666}, n_{999}). The shaded gray area shows the region of data that has been excluded from all calculations of nested domain statistics. Descriptions for all the runs in the legend can be found in Table 1.

3. Results

Comparisons between nested domains (n_{333}, n_{666}, n_{999}) and our stand-alone LES (p_{LES}) can help us assess whether or not the finger-prints of the spurious mesoscale structures adversely influence the LES. Therefore, the stand-alone LES represents a standard by which to evaluate the influence of the parent domains on nested LES in the idealized setting of this study. After a description of the TI mesoscale flow characteristics, we present an analysis of the streamwise development of the nested flow, followed by observations of first-order flow characteristics, turbulence strength, horizontal-vertical partitioning of turbulence, and structural characteristics of the LES convection.

3.1. Mesoscale Flow in the TI

The characteristics of the modeled mesoscale, TI flows are dependent on the PBL scheme [*Ching et al.*, 2014]. The results of our study are limited to the MYNN PBL scheme, but similar analyses could be performed using other available PBL parametrizations. Due to the PBL scheme horizontal grid-cell homogeneity assumption violations, the modeled TI mesoscale runs contain unrealistic, grid-size-dependent, convective cells [*Zhou et al.*, 2014; *Ching et al.*, 2014]. Figure 5 shows how the size of these structures increases with grid-cell size. More quantitative analysis can be performed by analyzing the turbulence statistics of the flow. Both mesoscale and microscale models contain subgrid-scale parametrizations, which are intended to represent the net effect of under-resolved fluctuations, those that are too small to be resolved by the computational grid, on the large-scale flows. For mesoscale models, vertical subgrid-scale motions are computed by a PBL scheme, while horizontal subgrid-scale motions are computed by a separate two-dimensional turbulent diffusion scheme. For LES, this SGS effect is computed by a turbulence closure scheme. LES are able to explicitly resolve the most energetic eddies, while the influence of the turbulent motions that are smaller than the grid-size is parametrized. Since LES have much higher resolutions than the mesoscale simulations, they are expected to resolve more of the turbulence and have lower levels of SGS turbulence than the mesoscale runs. The SGS parametrizations produce values of SGS TKE, heat flux, and Reynolds stress. The total amount of modeled turbulence in
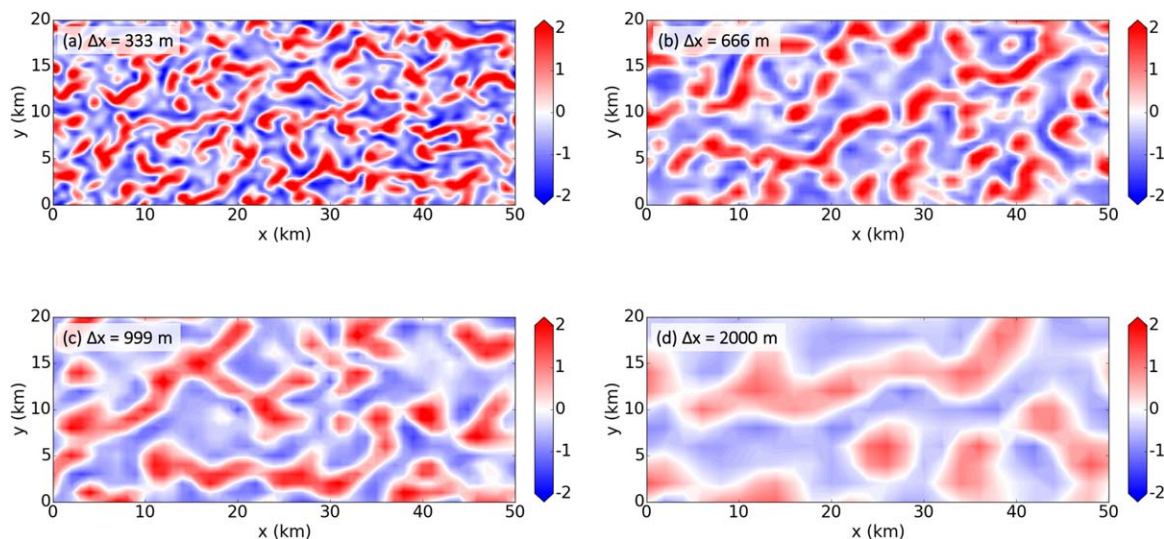

Figure 5. Horizontal contours of vertical velocity, w (m s^{-1}), after 10 h of simulation and at a height of $z = 1000$ m, for four TI mesoscale runs with different grid-cell sizes, $\Delta x = \Delta y =$ (a) 333 m, (b) 666 m, (c) 999 m, and (d) 2000 m.
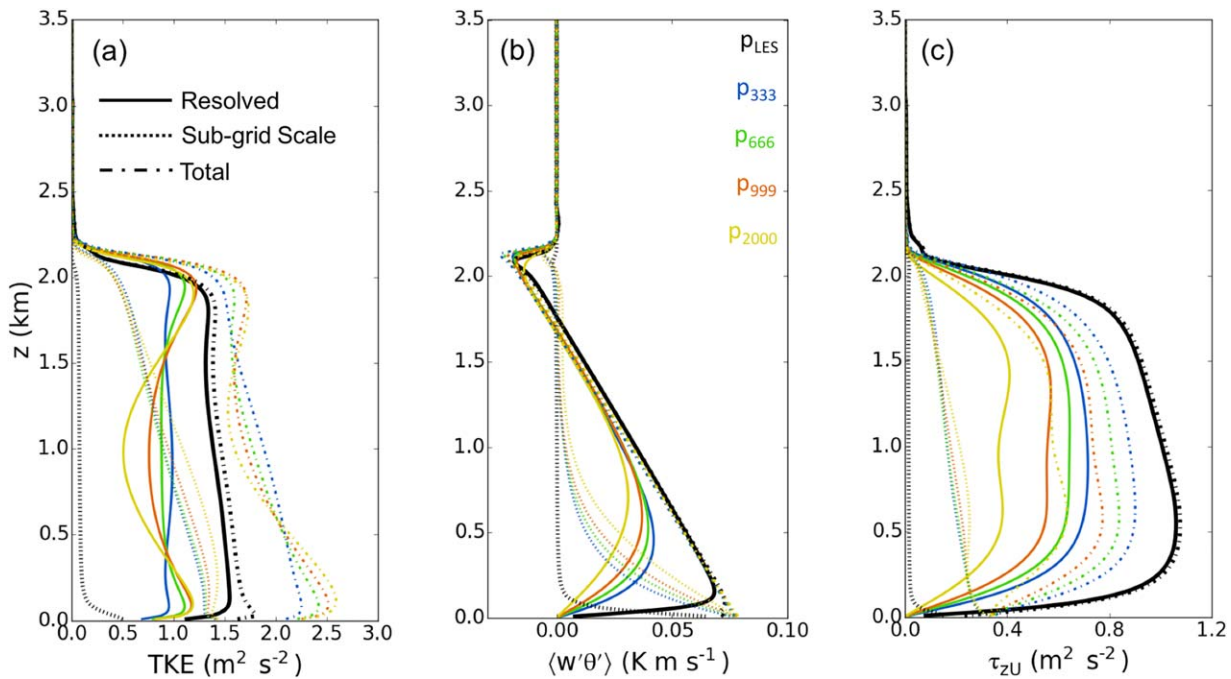
Figure 6. Horizontally averaged vertical profiles of resolved: (a) TKE, (b) vertical heat flux, (c) Reynolds stress, $\tau_z = \sqrt{\langle w'u' \rangle^2 + \langle w'v' \rangle^2}$. Time averages were performed for the last 3 h of simulation all of the cases.

the flow is the sum of the resolved and SGS contributions. In our simulations, the resolved mesoscale flows are characterized by lower TKE, heat flux ($\langle w'\theta' \rangle$), and Reynolds stress ($\tau_{zU}$) throughout the PBL as can be seen in Figure 6. The turbulence quantities have been horizontally and temporally averaged for the measurement time period shown in Figure 1. These low levels of turbulence can be partly expected from the coarser resolution of these mesoscale simulations, since smaller turbulence length scales cannot be resolved by such coarse grids. However, there are certain characteristics that cannot be explained by the lower resolution. For example, the difference between the TKE in the middle and near the top and bottom of the PBL increases with decreasing resolution. Additionally, we can see that the subgrid-scale values of TKE and τ_{zU} do not take into account the differences in the resolved turbulent energy, resulting in variable values of total TKE and τ_{zU} which are resolution-dependent. The total TKE for the mesoscale runs is up to ~60% higher than the stand-alone LES TKE, while the total τ_{wU} is up to ~30% lower in all the mesoscale runs than it is in the stand-alone LES. The resolved flow characteristics are applied to the x and y boundaries of the nested LES domain.
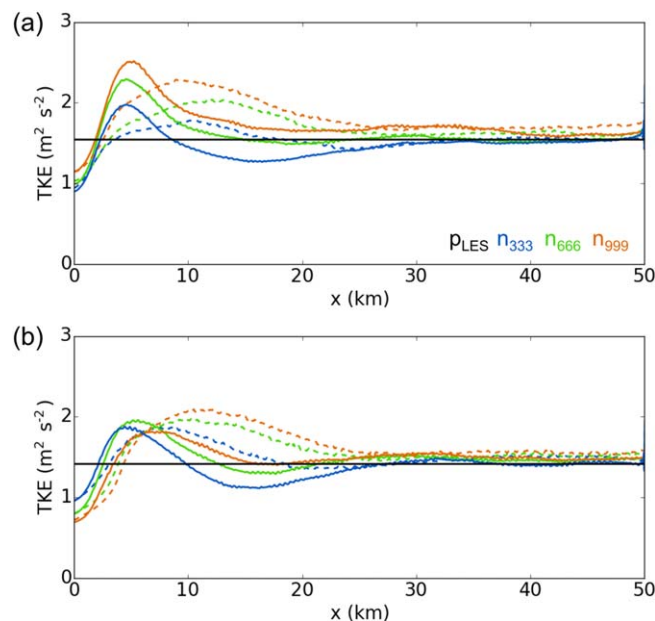

Figure 7. Time- and y-averaged, resolved TKE for the nested simulations and for the stand-alone LES (x-averaged) as a function of distance downstream of the inflow boundary, x, at two different heights, (a) $z = 250$ m and (b) 1000 m. ($^{---}$) Represents the nested simulations without boundary perturbations (n_{333np}, n_{666np}, n_{999np}).
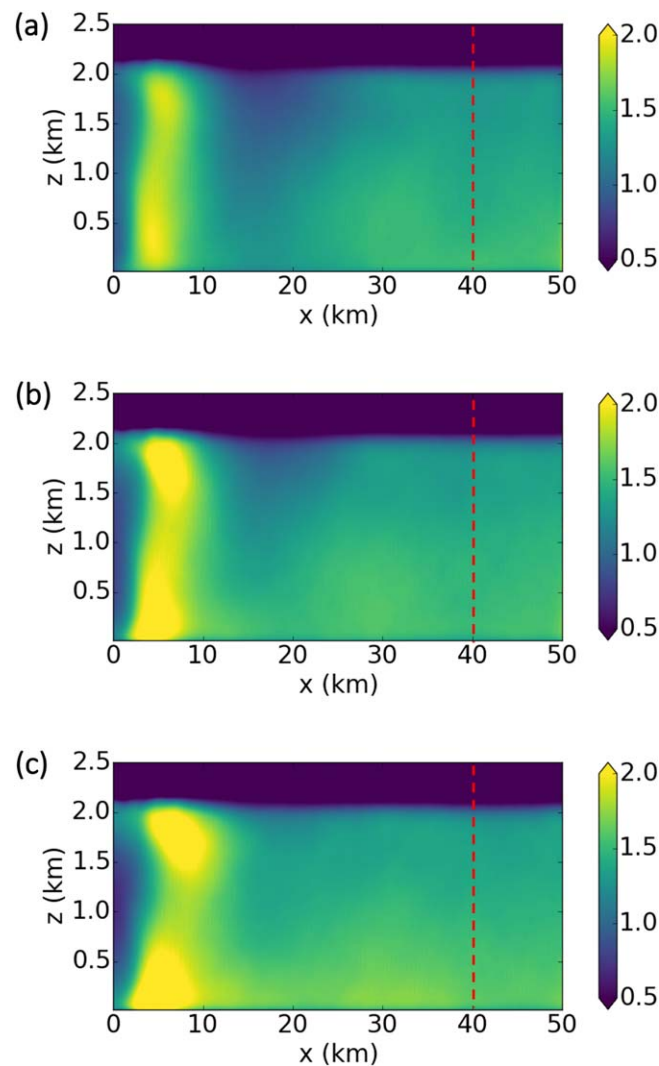
Figure 8. Vertical contours showing the x-evolution of time- and y-averaged, resolved TKE for our three nested simulations: (a) n_{333}, (b) n_{666}, and (a) n_{999}. The dashed red lines represent the location used for further comparisons of flow statistics with the stand-alone LES domain, p_{LES}.

3.2. Spatial Flow Development

As the mesoscale flow structures travel through the nested LES domain, they are broken down by the resolved and SGS turbulence developed by the LES. Convective structures continue to change with x location until the flow reaches a developed state, defined as the x location at which the streamwise fluctuations of resolved TKE are smaller than ∼5%. Figure 7 shows the evolution of resolved, y and time-averaged TKE in the x direction for the nested simulations at two heights within the PBL, $z = 250$ and 1000 m. The effect of the cell perturbations on the spatial flow evolution of the nested domains is also shown in this figure by comparing perturbed (—) and unperturbed (- - -) domains with the same parent resolution. For the case with the coarsest parent resolution, n_{999np}, the unperturbed simulation requires close to twice the distance as the perturbed simulation to reach a stable value of resolved TKE. The unperturbed case n_{666np} reaches a stable resolved TKE after a slightly shorter distance than n_{999np}, and case n_{333np} takes approximately the same distance as the perturbed simulation. Additionally, n_{999np} overestimates resolved TKE by ∼20% through the end of the domain when compared to p_{LES}, while n_{999} shows only a ∼10% higher resolved TKE than n_{LES}. This TKE overestimation of the unperturbed simulations de-

creases with decreasing parent grid-cell sizes: n_{333}, n_{333np}, and n_{LES} develop nearly identical resolved TKE values beyond $x = 30$ km. Although the cell perturbation method was developed for the transition between smooth mesoscale flows and LES, our results show that it is also beneficial when the mesoscale domain contains under-resolved convection. We have also shown that the effect of the cell perturbations on the nested flows is dependent on the nature of the parent flows.

Previous studies have concluded that turbulence generation methods are necessary when LES boundary conditions contain much lower levels of turbulence than the levels that will be developed by the LES [*Tabor and Baba-Ahmadi*, 2010; *Zajaczkowski et al.*, 2011; *Mirocha et al.*, 2014; *Muñoz-Esparza et al.*, 2014a, 2014b]. Due to this need for turbulence generation and the results presented above, we base our upcoming analysis on the three perturbed cases n_{333}, n_{666}, and n_{999}.

At $z = 1000$ m all three of the nested simulations converge to resolved TKE ∼ 1.5 m^2 s^{-2} by $x \sim 30$ km. However, while the same convergence length is observed for n_{333} and n_{666} at $z = 250$ m, a longer fetch of ∼40 km is necessary for convergence of the nested simulation with the coarsest parent, n_{999}. The three nested simulations have a peak in TKE at $x \sim 5$ km. This peak shows a z-dependence which increases with the mesoscale grid-size. The resolved TKE difference for the maximums at the two heights is ∼0.7 m^2 s^{-2}
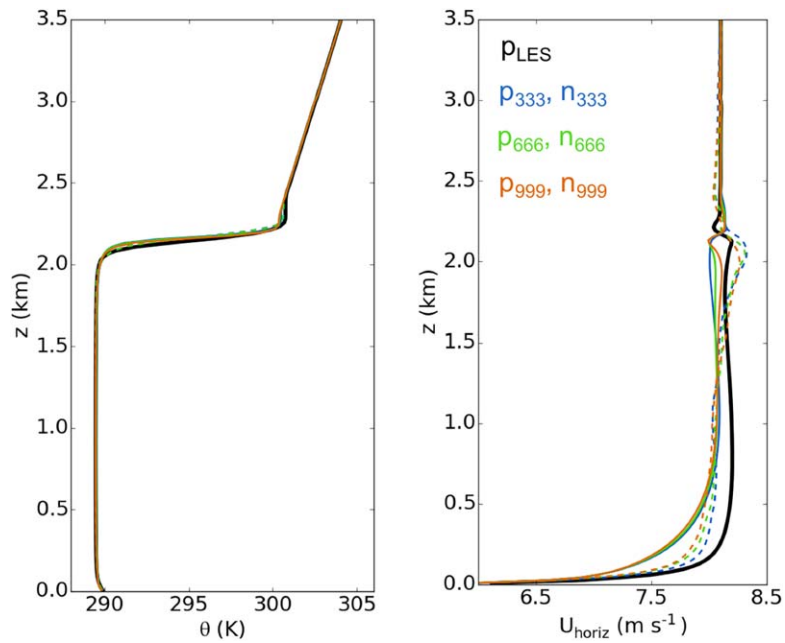
Figure 9. Vertical profiles of (a) potential temperature, θ, and (b) horizontal velocity, U_{horiz} for all of the simulations. All of the simulations have been time- and y-averaged. Solid lines (—) represent periodic domains, with x-averaged conditions. Dashed lines (- - -) represent nested domains, for which statistics were found at $x = 40$ km.

for n_{999}, ~0.4 m^2 s^{-2} for n_{666}, and ~0.1 m^2 s^{-2} for n_{333}. Figure 8 shows vertical contours of the x-evolution of resolved TKE, in which this vertical variation can be seen more clearly. For the simulation with the highest parent resolution, n_{333}, the initial increase of resolved TKE occurs in a relatively uniform way throughout the PBL height. As the parent resolution decreases, this rapid increase in resolved TKE is distributed closer to the top and bottom of the PBL, with a region in the center of the PBL showing a less dramatic increase.
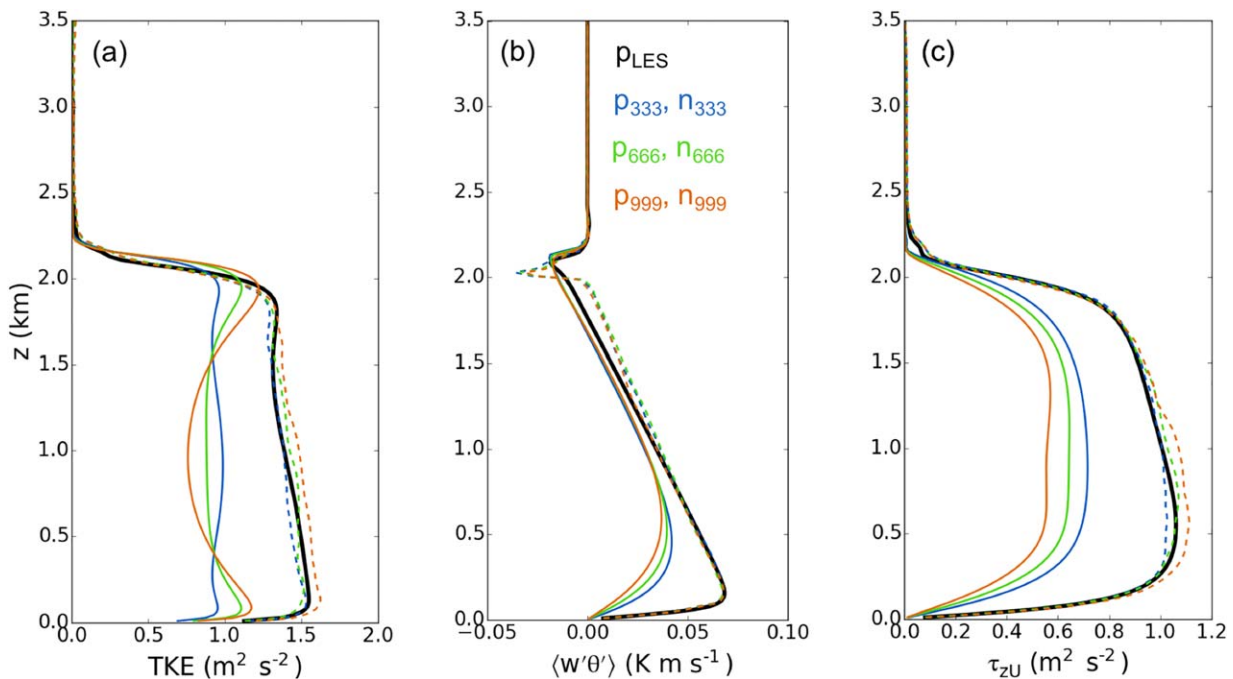

Figure 10. Vertical profiles of time- and y-averaged, resolved (a) TKE, (b) vertical heat flux, and (c) Reynolds stress or vertical transport of horizontal momentum. Solid lines (—) represent periodic domains, with x-averaged conditions. Dashed lines (- - -) represent nested domains, for which statistics were found at $x = 40$ km.

These observations correspond well with the TKE inflections observed in Figure 5a, indicating that the resolved TKE from the parent domains affects the behavior of the flow while it adapts to the finer resolution, but it does not have a significant effect on the rate of this equilibration.

The location at $x = 40$ km (red dashed line in Figure 8) was selected to represent the final, converged flow in subsequent evaluations. In the following sections, we compare nested flow statistics at this location with x-averaged statistics from the stand-alone LES to find whether parent domain differences endure past the adaptation region.

3.3. First-Order Flow Characteristics

The vertical profile of potential temperature, θ, depends on both the strength of the forcing heat flux, and whether or not the PBL is well mixed. Since the same convective forcing drives all of the simulations, we expect the vertical profiles of θ to be very similar for all the simulations. This is confirmed in Figure 9a, which shows that profiles of θ from the mesoscale simulations are nearly identical to that of the stand-alone LES, consistent with the observations of *Zhou et al.* [2014] and *Shin and Dudhia* [2016]. Additionally, profiles of θ from the nested simulations are also nearly identical to the stand-alone LES profile.

The profiles of horizontal wind speed, U_{horiz} exhibit slightly more variability than the profiles of potential temperature (Figure 9b). The mesoscale simulations have $\sim$10% lower horizontal speeds throughout the PBL and lower shear near the surface than the stand-alone LES. These differences are most likely caused by the MYNN PBL parametrization, and to a minor extent by differences in the implementation of the Monin-Obukhov surface layer parameterizations specific to each PBL formulation in WRF. Therefore, different PBL schemes may potentially affect these results. At $x = 40$ km, the nested simulations present higher horizontal wind speeds than the mesoscale parents. However, these wind speeds are still $\sim$3% lower than the wind speeds obtained in the stand-alone LES, evidencing a weak influence of the low parent domain wind speeds. A weak grid-size dependence can be observed: the nest with the finest parent resolution, n_{333}, has higher horizontal wind-speeds than the other two nested LES (n_{666} and n_{999}). Finally, the nested LES are able develop a higher wind shear near the bottom boundary that more strongly resembles the wind-shear in the reference simulation, n_{LES}.
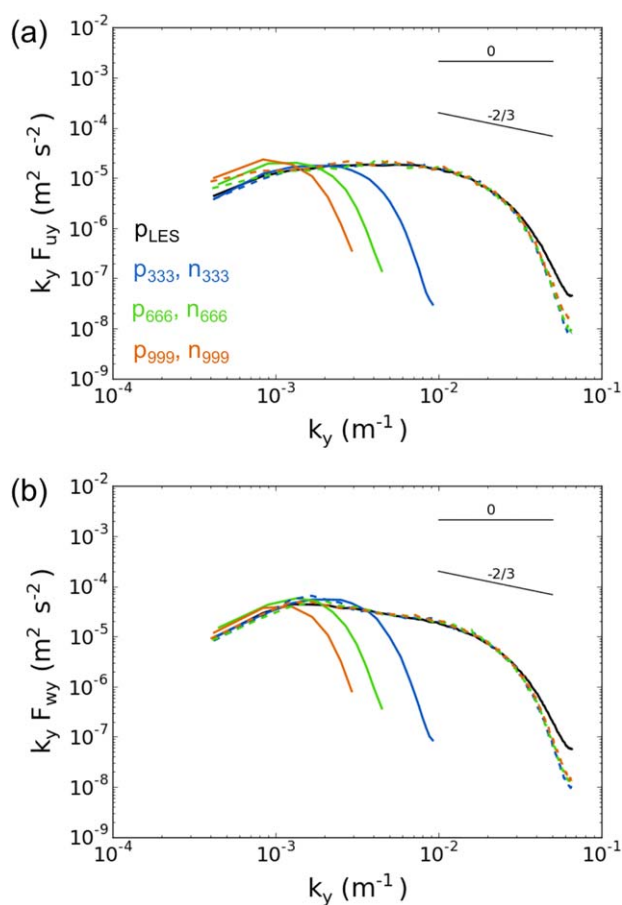
3.4. Turbulence Characteristics

All of the nested simulations contain nearly identical levels of SGS turbulence (not shown). Therefore, the turbulent quantities in all upcoming analysis refer to resolved quantities unless otherwise specified, and comparisons of these quantities are also valid for total levels of turbulence. All three nested simulations generated vertical distributions of TKE that match the stand-alone simulation (Figure 10a). For n_{333} and n_{666}, TKE matches the stand-alone profile almost exactly, suggesting that higher parent resolutions help to better represent the vertical distribution of

Figure 11. Turbulent spectra of (a) horizontal velocity and (b) vertical velocity in the y direction at a height $z = 1000$ m. Spectra for the periodic simulations was averaged in the x direction. Solid lines (—) represent periodic domains, with x-averaged conditions. Dashed lines (- - -) represent nested domains, for which statistics were found at $x = 40$ km. Lines with slopes of 0 and $-2/3$ are shown for reference.

TKE in the nested LES domains. The nested simulation with the coarsest parent domain, n_{999}, exhibits a small overestimation of up to $\sim$10% for TKE throughout the PBL. This overestimation is directly proportional to the parent grid-size.

The profiles of vertical heat flux, $\langle w'\theta' \rangle$, for all of the nested simulations also match the stand-alone LES profile in the bottom half of the PBL (Figure 10b). However, in the top half of the PBL, all of the nested simulations slightly overestimate heat flux by up to $\sim$0.01 K m s^{-1}. Although we have not determined the cause of this overestimation, we would like to caution users to this feature, since no optimal resolution was found to address it. The behavior of the Reynolds stress profiles, τ_{zU}, is similar to that of the TKE profiles (Figure 10c), with a very small systematic overestimation ($\sim$8%) of vertical transport of horizontal momentum with increasing grid-cell size.

The superior performance of the n_{333} simulation is further reinforced by the turbulent spectra of velocity at $z = 1000$ m and $x = 40$ km, shown in Figure 11. The turbulent spectra of horizontal velocity in the y direction, $k_y F_{uy}$ (Figure 11a), shows an increase in energy at small wavenumbers for the coarser nested simulations, n_{666} and n_{999}, that coincides with a corresponding high energy from their parent domains, p_{666} and p_{999}. This effect can be seen at all heights (only $z = 1000$ m is shown), although it is weaker in the nested simulations for heights very close to the surface. This higher energy at low wavenumbers is not present in the n_{333} or p_{333} simulations, and n_{333} shows an exact match with the stand-alone LES turbulent spectra except for the very finest scales, at which numerical dissipation takes place. Differences at high wavenumbers are not relevant for this analysis, as they represent numerical dissipation differences caused by a 10° shift in the direction of horizontal speed between the stand-alone and nested simulations.

Despite the slight overestimations in TKE, heat flux, and Reynolds stress, the nested simulation profiles are remarkably close to the stand-alone LES profiles. However, although all of the nested simulations are given boundary conditions with much lower turbulence stresses, the two highest-resolution mesoscale simulations are able to provide the profiles with the closest vertical distribution to our reference case. This appears to have a positive, if mild, effect on the nest's performance.

3.5. Horizontal and Vertical Turbulence Partitioning

The partitioning of turbulent energy between the vertical and horizontal directions can have significant mixing and transport implications. To assess whether the effects observed in section 3.4 are more pronounced in one
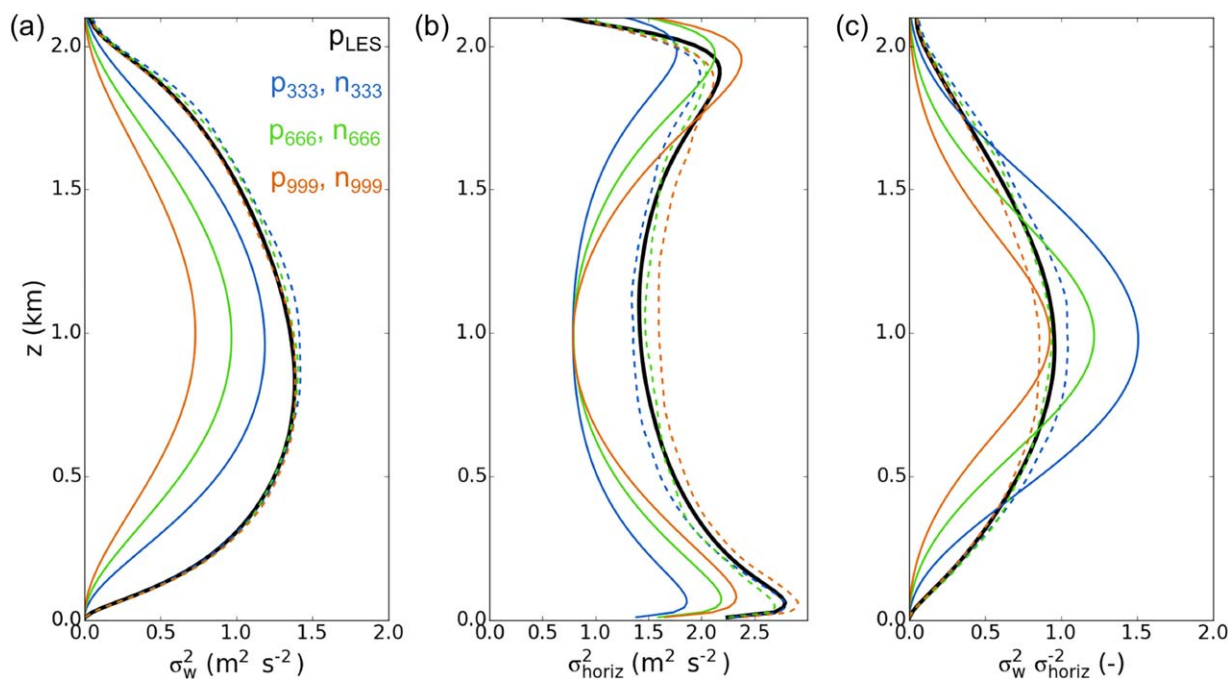

Figure 12. Time- and y-averaged profiles of (a) vertical variance, (b) horizontal variance, and (c) ratio between vertical and horizontal variance. Solid lines (—) represent periodic domains, with x-averaged conditions. Dashed lines (- - -) represent nested domains, for which statistics were found at $x = 40$ km.
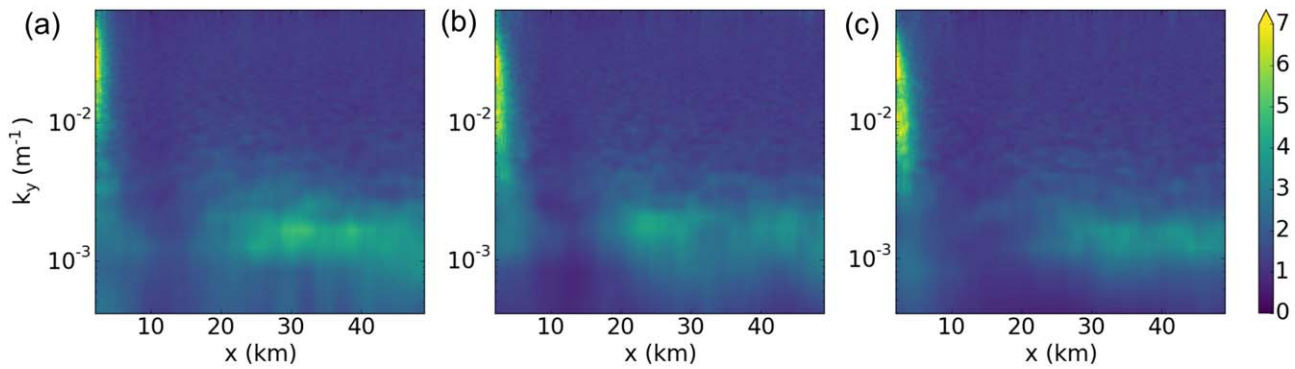
Figure 13. Contours of the time-averaged ratio between the vertical and horizontal velocity spectra (F_{wy}/F_{uy}), as a function of x and wavenumber, k_y. (a) n_{333}, (b) n_{666}, and (c) n_{999}.

direction than the other, the horizontal and vertical variances, σ^2_{horiz} and σ^2_w, respectively, are analyzed separately (Figures 12a and 12b). In the mesoscale parent simulations, the grid-size dependence of TKE near the center of the PBL is caused by differences in σ^2_w for different mesoscale grid resolutions, while near the top and bottom boundaries of the PBL it is more greatly influenced by σ^2_{horiz}. For the nested simulations, n_{999} matches the vertical variance of the stand-alone simulation exactly, while n_{666} and n_{333} very slightly overestimate the vertical variance ($\sim$1%). This pattern is the opposite of the pattern for TKE, indicating that the grid-size dependence observed in the TKE profiles is most significantly influenced by the grid-size dependence in the horizontal than the vertical variance.

The relative strength of the vertical to horizontal turbulent motions can be represented by the ratio of the vertical to horizontal variances, $\sigma^2_w/\sigma^2_{horiz}$ (Figure 12c). For the stand-alone LES, $\sigma^2_w/\sigma^2_{horiz}$ is nearly 1 near the middle of the PBL, indicating near-isotropic turbulence in this region. This ratio decreases near the top and bottom of the PBL, indicating a greater influence of the horizontal variance, relative to the vertical variance. Near these regions, the temperature inversion and the surface inhibit vertical fluctuations.

For the parent simulations, $\sigma^2_w/\sigma^2_{horiz}$ increases with decreasing grid-cell size, with p_{999} being the only mesoscale run that was able to reach near isotropic conditions, $\sigma^2_w/\sigma^2_{horiz} = 1$, in the middle of the PBL, while p_{666} and p_{999} show a higher vertical variance relative to the horizontal variance in this region. This grid-size dependence occurs throughout the PBL, with $\sigma^2_w/\sigma^2_{horiz}$ being lowest for n_{999} and highest for n_{333}. A similar grid-size dependence appears for the nested simulations, with n_{333} showing the highest variance ratio, followed by n_{666} and then n_{999}. However, in spite of these differences, all three nested runs are close to isotropic near the center of the PBL, and none of them show regions of higher vertical than horizontal variance. Finally, when compared with the variance ratio for the stand-alone LES, n_{666} shows the closest ratio of vertical to horizontal variance as compared to the other two nested simulations.

3.6. Convective Structure Characteristics

Convective structures in the simulated flows can be characterized by different length scales. One of these scales can be found by further exploring the peak in partitioning of vertical and horizontal turbulence through the ratio between the turbulent energies, F_{wy}/F_{uy}, as a function of wavenumber. Figure 13 shows this ratio for all three of our nested simulations. There is an area of very high F_{wy}/F_{uy} for high wavenumbers near the inflow
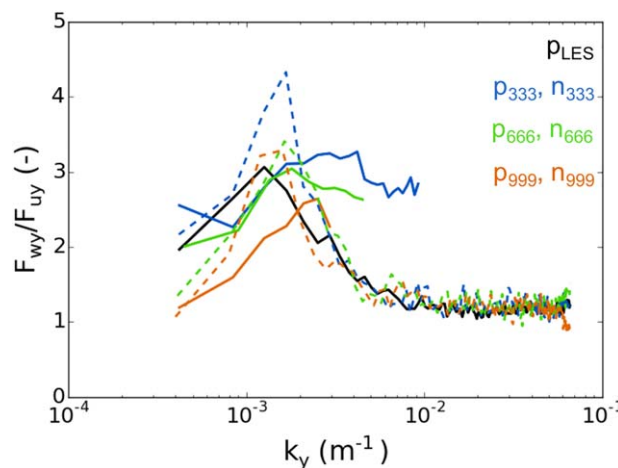

Figure 14. Ratio between vertical and horizontal turbulent energy spectra for all of the simulations. Solid lines (—) represent periodic domains, with x-averaged conditions. Dashed lines (- - -) represent nested domains, for which statistics were found at $x = 40$ km.
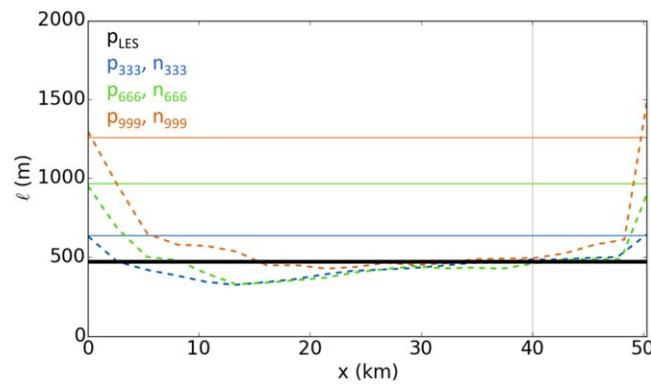
Figure 15. Spatial evolution of the length scale of convective structures, ℓ, corresponding to the separation value for which the auto-correlation is $R(\ell) = R(0)/e$. Solid lines (—) represent periodic domains, with x-averaged conditions. Dashed lines (- - -) represent nested domains.

boundary. These small, energetic turbulent motions that are stronger in the vertical than the horizontal direction represent the effect of the temperature perturbations from the cell perturbation method, and the small motions triggered by them. There is no evidence of a high F_{wy}/F_{uy} at such high wavenumbers, indicating that the perturbations have no effect on the vertical to horizontal partitioning of the developed flow.

As the flow moves through the domain the high F_{wy}/F_{uy} caused by the cell perturbations rapidly decreases, and after about 20–25 km, a region of slightly higher F_{wy}/F_{uy} develops for wavenumbers close to 1.5×10^{-3} m^{-1} for all the nested LES, and approximately 1.2×10^{-3} m^{-1} for the stand-alone LES. Figure 14 provides a comparison of F_{wy}/F_{uy} at $x = 40$ km, showing these peaks, which represent the scale for which vertical fluctuations are most energetic relative to horizontal ones. For n_{333}, this peak has a higher value than for the rest of the LES simulations, indicating that for this case, vertical turbulent motions are most energetic when compared to horizontal turbulent motions. However, this higher ratio is produced by a slightly higher energy in the turbulent spectra of vertical velocity for the corresponding wavenumber (Figure 11b). The wavenumbers ($k_y = 2\pi/\lambda_y$) corresponding to these maximum vertical to horizontal turbulent energy ratios can be attributed to wavelengths of $\lambda_y \sim 4200$ m for the nested LES and ~ 5200 m for the stand-alone LES. This scale is comparable to the diameter of the convective cells observed in both the nested domains at $x \sim 40$ km (Figure 6), and for our stand alone LES (Figure 2), and it includes both updraft and downdraft regions. This result indicates that nested LES present convective structures that are $\sim 20\%$ smaller than expected by our reference stand-alone LES.

To further analyze the size of the convective structures, the auto-correlation, R, of the vertical velocity, w, is calculated along the y direction for all simulations. The scale of correlation decay can be interpreted as a mean measure of the thickness of individual updraft and downdraft regions of the flow. This value is quantified through a length scale, ℓ, defined here as the separation parameter for which the correlation is $R(\ell) = 1/e$. Figure 15 presents the evolution of ℓ in the x direction for the nested domains, as well as the x-averaged values of ℓ for the cyclic domains. For the mesoscale simulations, we observe a systematic decrease in ℓ with decreasing grid-cell size. This indicates that the mean thickness of updraft and downdraft regions decreases with increasing resolution, with p_{333} presenting the closest ℓ to the reference simulation, p_{LES}. The nested simulations show differences in the evolution of ℓ with distance, x: the nest with the coarsest parent resolution, n_{999}, shows a developed value of ℓ by $x \sim 15$ km, while n_{666} and n_{999} do not show this development until ℓ by $x \sim 30$ km. At $x = 40$ km ℓ is nearly identical for all of the LES, $\ell \sim 500$ m, indicating that the draft thickness of the developed convective structures in the nested domains are not affected by the draft thickness of structures in the parent simulations.

4. Summary and Future Work

In this study, we assess the performance of an LES nest within a mesoscale parent at TI resolution in a dry convective boundary layer (CBL). In mesoscale-to-LES grid-nesting, the mesoscale, parent simulation is often run at resolutions within the terra incognita (TI). These resolutions are too high for the models' design specifications, resulting in the presence of unrealistic flow characteristics in the mesoscale-modeled CBL. Three nested mesoscale-to-LES runs were performed with different parent resolutions within the TI. The characteristics of the nested LES flows were compared with those of a stand-alone LES domain to determine whether nested microscale simulations are able to overcome the potential bias caused by these unrealistic characteristics.

We found that the behavior of certain quantities in the nested LES does not depend on parent resolution. For example, mean profiles of potential temperature (θ) are nearly identical for all of the simulations, which is expected for well-mixed boundary layers that have the same surface heat flux. Horizontal wind shear near the surface for all of the nested domains closely resembles the reference, stand-alone LES, n_{LES}. Vertical profiles of turbulent heat flux showed a slightly overestimated flux of ∼0.01 K m s^{-1} in the top half of the boundary layer that is independent of the parent resolution. From a structural perspective, we found that nested convective cells have a smaller diameter than stand-alone LES cells by ∼20%, with all of the nested simulations showing an estimated cell diameter ∼4200 m, and our stand-alone LES having a cell diameter ∼5200 m. Additionally, an estimated updraft/downdraft thickness of ∼500 m was found for both nested and stand-alone LES.

However, parent resolution had a significant effect on the fetch necessary to generate TKE as the flow moves through the domain: resolved TKE for n_{333} and n_{666} converges after fetches of $x \sim 30$ km from the inflow boundary at heights, while TKE convergence for n_{999} required $x \sim 40$ km near the surface. Based on this observation, nested flow statistics have been calculated at $x = 40$ km, including first-order quantities (θ and U_{horiz}), resolved turbulent statistics (TKE, $\langle w'\theta' \rangle$ and τ_{zU}) and convective structure size. A parent grid-size dependence of the nested LES is also observed in horizontal wind speeds, which are ∼3% lower than the horizontal wind speeds of the stand-alone LES throughout the PBL for all of the nested domains. n_{333} has the smallest wind speed differences from p_{LES}, and the difference systematically increases with parent grid-cell size as we go to n_{666} and n_{999}. The effects of the parent domain on the resolved TKE and τ_{zU} statistics also depend on the parent grid-cell size. Of the three simulations performed in this study, the nested simulation with the finest parent resolution, n_{333}, performs the best overall for the representation of these quantities. For n_{333} and n_{666}, both vertical profiles of resolved TKE and τ_{zU} are nearly identical to the reference LES profile. The simulation with the greatest parent grid-cell size, n_{999}, shows slightly overestimated resolved TKE and τ_{wU} profiles, although the shapes of the profiles strongly resemble the reference profile. This overestimation of turbulent energy is influenced more significantly by horizontal than vertical variances, suggesting that the grid-size dependency is related to the development of turbulent energy in the horizontal direction. In spite of this, we find that the magnitudes of vertical variance are larger than those of horizontal variance throughout the PBL, with a nearly isotropic region of turbulence around the middle of the PBL for all of the LES runs.

Our results show that, given adequate fetch, nested LES can recover from unrealistic conditions being imposed through the simulation boundaries, including low levels of resolved TKE, heat flux and Reynolds stress, unrealistic vertical distributions of TKE with higher values near the surface and temperature inversion than near the midpoint of the PBL, and large, under-resolved convective cells. This fetch has been reduced by using the cell-perturbation method on the nested domains. Based on our observations, we recommend using the highest parent resolution permitted by computational resource availability when modeling a strongly convective ABL to reduce the fetch of turbulence development, produce the most accurate convective structures, and avoid overestimating turbulence strength. We would also like to direct caution to the low horizontal wind speeds and to the high vertical heat flux present in the top half of the PBL for all of the nested simulations. These discrepancies would not be problematic for studies that concern the lower half of the PBL such as wind energy and fire propagation studies.

These simulations focus on strong convection. In weaker convection, neutrally stratified, or stable simulations, it remains to be seen if the fingerprints of parent mesoscale simulations persist into the nested microscale simulations. A similar study for the case of weaker convection, with the presence of convective rolls rather than cells, may show that the alignment of the convective structures with the flow, as well as the weaker convective mixing, has an effect in the recovery of the nested LES. It is also possible to perform nested mesoscale-LES simulations in which both the parent mesoscale and nested LES domains have resolutions in the TI. This particular TI-mesoscale to TI-LES setup may show a different performance than was shown in this study, as additional assumptions are violated within the LES closure scheme. Furthermore, scale-aware parametrizations [*Shin and Hong*, 2014] and three-dimensional PBL schemes are being developed to provide more reliable turbulence models in the TI. Until these schemes are fully developed and implemented, microscale nests will continue to be nested within unrealistic mesoscale parents. Additionally, mesoscale simulations in our study were performed using the MYNN PBL scheme. Our study provides general guidelines for nesting LES within mesoscale simulations at TI resolutions, but the nature of the modeled TI mesoscale flows is expected to depend upon the choice of PBL parametrization, as shown by *Ching et al.* [2014].

We have shown that nesting LES within mesoscale models in the CBL has great value despite the challenges presented. Nested LES domains are able to significantly overcome the unrealistic flow features introduced by parent conditions while accurately modeling the fine scales of the flow. Therefore, we positively recommend this as a method to include large-scale conditions in microscale simulations of multiscale CBL processes.

References

Aitken, M. L., B. Kosović, J. D. Mirocha, and J. K. Lundquist (2014), Large eddy simulation of wind turbine wake dynamics in the stable boundary layer using the Weather Research and Forecasting Model, *J. Renewable Sustainable Energy*, *6*(3), 033137, doi:10.1063/1.4885111.

Beare, R. J. (2013), A length scale defining partially-resolved boundary layer turbulence simulations, *Boundary Layer Meteorol.*, *151*(1), 39–55, doi:10.1007/s10546-013-9881-3.

Calaf, M., C. Meneveau, and J. Meyers (2010), Large eddy simulation study of fully developed wind-turbine array boundary layers, *Phys. Fluids*, *22*(1), 015110, doi:10.1063/1.3291077.

Cheng, A., K.-M. Xu, and B. Stevens (2010), Effects of resolution on the simulation of boundary layer clouds and the partition of kinetic energy to subgrid scales, *J. Adv. Model. Earth. Syst.*, *2*(1), 3, doi:10.3894/JAMES.2010.2.3.

Ching, J. R., M. Rotunno, A. LeMone, B. Martilli, B. Kosović, P. A. Jimenez, and J. Dudhia (2014), Convectively induced secondary circulations in fine-grid mesoscale numerical weather prediction models, *Mon. Weather Rev.*, *142*(9), 3284–3302, doi:10.1175/MWR-D-13-00318.1.

Chow, F. K., and R. L. (2009), Evaluation of turbulence closure models for large-eddy simulation over complex terrain: Flow over Askervein hill, *J. Appl. Meteorol. Climatol.*, *48*(5), 1050–1065, doi:10.1175/2008JAMC1862.1.

Daniels, M. H., K. A. Lundquist, J. D. Mirocha, D. J. Wiersema, and F. K. Chow (2016), A new vertical grid nesting capability in the Weather Research and Forecasting (WRF) Model, *Mon. Weather Rev.*, *144*(10), 3725–3747, doi:10.1175/MWR-D-16-0049.1.

Deardorff, J. W. (1972), Numerical investigation of neutral and unstable planetary boundary layers, *J. Atmos. Sci.*, *29*(1), 91–115, doi:10.1175/1520-0469(1972)029<0091:NIONAU>2.0.CO;2.

Efstathiou, G. A., and R. J. Beare (2015), Quantifying and improving sub-grid diffusion in the boundary layer grey zone, *Q. J. R. Meteorol. Soc.*, *141*(693), 3006–3017, doi:10.1002/qj.2585.

Fernando, H. J. S. (2010), Fluid dynamics of urban atmospheres in complex terrain, *Annu. Rev. Fluid Mech.*, *42*(1), 365–389, doi:10.1146/annurev-fluid-121108-145459.

Fernando, H. J. S., S. M. Lee, J. Anderson, M. Princevac, E. Pardyjak, and S. Grossman-Clarke (2001), Urban fluid mechanics: Air circulation and contaminant dispersion in cities, *Environ. Fluid Mech.*, *1*(1), 107–164, doi:10.1023/A:1011504001479.

Honnert, R., V. Masson, and F. Couvreux (2011), A diagnostic for evaluating the representation of turbulence in atmospheric models at the kilometric scale, *J. Atmos. Sci.*, *68*(12), 3112–3131, doi:10.1175/JAS-D-11-061.1.

Honnert, R., F. Couvreux, V. Masson, D. Lancz (2016), Sampling the structure of convective turbulence and implications for grey-zone parametrizations, *Boundary Layer Meteorol.*, *160*(1), 133–156, doi:10.1007/s10546-016-0130-4.

Klemp, J. B., J. Dudhia, and A. D. Hassiotis (2008), An upper gravity-wave absorbing layer for NWP applications, *Mon. Weather Rev.*, *136*(10), 3987–4004, doi:10.1175/2008MWR2596.1.

Kosović, B. (1997), Subgrid-scale modelling for the large-eddy simulation of high-Reynolds-number boundary layers, *J. Fluid Mech.*, *336*, 151–182, doi:10.1017/S0022112096004697.

Liu, Y., T. Warner, Y. Liu, C. Vincent, W. Wi, B. Mahoney, S. Swerdlin, K. Parks, and J. Boehnert (2011), Simultaneous nested modeling from the synoptic scale to the LES scale for wind energy applications, *J. Wind Eng. Ind. Aerodyn.*, *99*(4), 308–319, doi:10.1016/j.jweia.2011.01.013.

Lundquist, K. A., F. K. Chow, and J. K. Lundquist (2012), An immersed boundary method enabling large-eddy simulations of flow over complex terrain in the WRF Model, *Mon. Weather Rev.*, *140*(12), 3936–3955, doi:10.1175/MWR-D-11-00311.1.

Michioka, T., and F. K. Chow (2008), High-resolution large-eddy simulations of scalar transport in atmospheric boundary layer flow over complex terrain, *J. Appl. Meteorol. Climatol.*, *42*(12), 3150–3169, doi:10.1175/2008JAMC1941.1.

Mirocha, J., J. K. Lundquist, and B. Kosović (2010), Implementation of a nonlinear subfilter turbulence stress model for large-eddy simulation in the advanced research WRF Model, *Mon. Weather Rev.*, *138*(11), 4212–4228, doi:10.1175/2010MWR3286.1.

Mirocha, J., B. Kosović, and G. Kirkil (2014), Resolved turbulence characteristics in large-eddy simulations nested within mesoscale simulations using the Weather Research and Forecasting Model, *Mon. Weather Rev.*, *142*(2), 806–831, doi:10.1175/MWR-D-13-00064.1.

Miyamoto, Y., Y. Kajikawa, R. Yoshida, T. Yamaura, H. Yashiro, and H. Tomita (2013), Deep moist atmospheric convection in a subkilometer global simulation, *Geophys. Res. Lett.*, *40*, 4922–4926, doi:10.1002/grl.50944.

Moeng, C.-H, J. Dudhia, J. Klemp, and P. Sullivan (2007), Examining two-way grid nesting for large eddy simulation of the PBL using the WRF model, *Mon. Weather Rev.*, *135*(6), 2295–2311, doi:10.1175/MWR3406.1.

Monin, A. S., and A. M. Obukhov (1954), Basic turbulence mixing laws in the atmospheric surface layer, *Tr. Inst. Teor. Geofiz., Akad. Nauk SSSR*, *24*(151), 163–187, doi:10.1007/s10546-015-0045-5.

Muñoz-Esparza, D., B. Kosović, C. Garcia-Sanchez, and J. van Beeck (2014a), Nesting turbulence in an offshore convective boundary layer using large-eddy simulations, *Boundary Layer Meteorol.*, *151*(3), 453–478, doi:10.1007/s10546-014-9911-9.

Muñoz-Esparza, D., B. Kosović, J. Mirocha, and J. van Beeck (2014b), Bridging the transition from mesoscale to microscale turbulence in numerical weather prediction models, *Boundary Layer Meteorol.*, *153*(3), 409–440, doi:10.1007/s10546-014-9956-9.

Muñoz-Esparza, D., B. Kosović, J. Mirocha, and J. van Beeck (2015), A stochastic perturbation method to generate inflow turbulence in large-eddy simulation models: Application to neutrally stratified atmospheric boundary layers, *Phys. Fluids*, *27*(3), 035102, doi:10.1063/1.4913572.

Muñoz-Esparza, D., J. A. Sauer, R. R. Linn, and B. Kosović (2016), Limitations of one-dimensional mesoscale PBL parameterizations in reproducing mountain-wave flows, *J. Atmos. Sci.*, *73*(7), 2603–2614, doi:10.1175/JAS-D-15-0304.1.

Muñoz-Esparza, D., J. K. Lundquist, J. A. Sauer, B. Kosović, and R. R. Linn (2017), Coupled mesoscale-LES modeling of a diurnal cycle during the CWEX-13 field campaign: From weather to boundary-layer eddies, *J. Adv. Model. Earth Syst.*, doi:10.1002/2017MS000960, in press.

Nakanishi, M., and M. Niino (2009), Development of an improved turbulence closure model for the atmospheric boundary layer, *J. Meteorol. Soc. Jpn.*, *87*(5), 895–912, doi:10.2151/jmsj.87.895.

Porte-Agel, F., Y.-T. Wu, H. Lu, and R. J. Conzemius (2011), Large-eddy simulation of atmospheric boundary layer flow through wind turbines and wind farms, *J. Wind Eng. Ind. Aerodyn.*, *99*(4), 154–168, doi:10.1016/j.jweia.2011.01.011.

Rai, R. K., L. K. Berg, B. Kosović, J. D. Mirocha, M. S. Pekour, and W. J. Shaw (2016), Comparison of measured and numerically simulated turbulence statistics in a convective boundary layer over complex terrain, *Boundary Layer Meteorol.*, *163*(1), 69–89, doi:10.1007/s10546-016-0217-y.

Sauer, J. A., D. Muñoz-Esparza, J. M. Canfield, K. R. Costigan, R. R. Linn, and Y.-J. Kim (2016), A large-eddy simulation study of atmospheric boundary layer influence on stratified flows over terrain, *J. Atmos. Sci.*, *73*(7), 2615–2632, doi:10.1175/JAS-D-15-0282.1.

Shin, H. H., and J. Dudhia (2016), Evaluation of PBL parameterizations in WRF at subkilometer grid spacings: Turbulent statistics in the dry convective boundary layer, *Mon. Weather Rev.*, *144*(3), 1161–1177, doi:10.1175/MWR-D-15-0208.1.

Shin, H. H., and S.-Y. Hong (2014), Representation of subgrid-scale turbulent transport in convective boundary layers at gray-zone resolutions, *Mon. Weather Rev.*, *143*(1), 250–271, doi:10.1175/MWR-D-14-00116.1.

Skamarock, W. C., J. B. Klemp, J. Dudhia, D. O. Gill, D. M. Barker, M. G. Duda, X.-Y. Huang, W. Want, and J. G. Powers (2008), A description of the advanced research WRF version 3, *NCAR Tech. Note, NCAR/TN-475+STR*, NCAR, Boulder, Colo., doi:10.1175/MWR2830.1.

Sullivan, P. P., and E. G. Patton (2011), The effect of mesh resolution on convective boundary layer statistics and structures generated by large-eddy simulation, *J. Atmos. Sci.*, *68*(10), 2395–2415, doi:10.1175/JAS-D-10-05010.1.

Sun, W.-Y., and C.-Z. Chang (1986), Diffusion model for a convective layer. Part I: numerical simulation of convective boundary layer, *J. Clim. Appl. Meteorol.*, *20*(10), 1445–1453, doi:10.1175/1520-0450(1986)025<1445:DMFACL>2.0.CO;2.

Tabor, G. R., and M. H. Baba-Ahmadi (2010), Inlet conditions for large eddy simulation: A review, *Comput. Fluids*, *39*(4), 553–567, doi:10.1016/j.compfluid.2009.10.007.

Talbot, C., E. Bou-Zeid, and J. Smith (2012), Nested mesoscale large-eddy simulations with WRF: Performance in real test cases, *J. Hydrometeorol.*, *13*(5), 1421–1441, doi:10.1175/JHM-D-11-048.1.

Taylor, D. M., F. K. Chow, M. Delkash, and P. T. Imhoff (2016), Numerical simulations to assess the tracer dilution method for measurement of landfill methane emissions, *Waste Manage.*, *56*, 298–309, doi:10.1016/j.wasman.2016.06.040.

Vanderwende, B. J., B. Kosović, J. K. Lundquist, and J. D. Mirocha (2016), Simulating effects of a wind-turbine array using LES and RANS, *J. Adv. Model. Earth Syst.*, *8*, 1376–1390, doi:10.1002/2016MS000652.

Warner, T. T., R. A. Peterson, and R. E. Treadon (1997), A tutorial on lateral boundary conditions as a basic and potentially serious limitation to regional numerical weather prediction, *Bull. Am. Meteorol. Soc.*, *78*(11), 2599–2617, doi:10.1175/1520-0477(1997)078<2599:ATOLBC>2.0.CO;2.

Wing, A. A., and K. A. Emanuel (2014), Physical mechanisms controlling self-aggregation of convection in idealized numerical modeling simulations, *J. Adv. Model. Earth. Syst.*, *6*(1), 59–74, doi:10.1002/2013MS000269.

Wyngaard, J. C. (2004), Toward numerical modeling in the "terra incognita," *J. Atmos. Sci.*, *61*(14), 1816–1826, doi:10.1175/1520-0469(2004)061<1816:TNMITT>2.0.CO;2.

Zajaczkowski, F. J., S. E. E. Haupt, and K. J. Schmehl (2011), A preliminary study of assimilating numerical weather prediction data into computational fluid dynamics models for wind prediction, *J. Wind Eng. Ind. Aerodyn.*, *99*, 320–329, doi:10.1016/j.jweia.2011.01.023.

Zhou, B., and F. K. Chow (2013), Nighttime turbulent events in a steep valley: A nested large-eddy simulation study, *J. Atmos. Sci.*, *70*(10), 3262–3276, doi:10.1175/JAS-D-13-02.1.

Zhou, B., J. S. Simon, and F. K. Chow (2014), The convective boundary layer in the terra incognita, *J. Atmos. Sci.*, *71*(7), 2545–2563, doi:10.1175/JAS-D-13-0356.1.